The Jo-In protein welding system is a relevant tool to create CBM-containing plant cell wall degrading enzymes

Louise Badruna, Vincent Burlat, Pierre Roblin, Thomas Enjalbert, Guy Lippens, Immacolata Venditto, Michael O'donohue, Cédric Montanier

The Jo-In protein welding system is a relevant tool to create CBM-containing plant cell wall degrading enzymes

Louise Badruna[1], Vincent Burlat[2], Pierre Roblin[3], Thomas Enjalbert[1], Guy Lippens[1], Immacolata Venditto[4], Michael J. O'Donohue[1], Cédric Y. Montanier[1]*

*Correspondence: cedric.montanier@insa-toulouse.fr; Tel. +33 (0)5 61 55 97 13

[1] TBI, Université de Toulouse, CNRS, INRAE, INSA, Toulouse, France

[2] Laboratoire de Recherche en Sciences Végétales, Université de Toulouse, CNRS, UPS, Toulouse INP, 24 chemin de Borde Rouge, 31320 Auzeville-Tolosane, France

[3] Laboratoire de Génie Chimique, Université de Toulouse, CNRS, INPT, UPS, Toulouse, France

[4] Institute for Cell and Molecular Biosciences, Newcastle University, Newcastle upon Tyne NE2 4HH, UK

Abstract:

Irrespective of their biological origin, most proteins are composed of several elementary domains connected by linkers. These domains are either functionally independent units, or part of larger multidomain structures whose functions are defined by their spatial proximity. Carbohydrate-degrading enzymes provide examples of a range of multidomain structures, in which catalytic protein domains are frequently appended to one or more non-catalytic carbohydrate-binding modules which specifically bind to carbohydrate motifs. While the carbohydrate-binding specificity of these modules is clear, their function is not fully elucidated. Herein, an original approach to tackle the study of carbohydrate-binding modules using the Jo-In biomolecular welding protein pair is presented. To provide a proof of concept, recombinant xylanases appended to two different carbohydrate-binding modules have been created and produced. The data reveal the biochemical properties of four xylanase variants and provide the basis for correlating enzyme activity to structural properties and to the nature of the substrate and the ligand specificity of the appended carbohydrate-binding module. It reveals that specific spatial arrangements favour activity on soluble polymeric substrates and that activity on such substrates does not predict the behaviour of multimodular enzymes on insoluble plant cell wall samples. The results highlight that the Jo-In protein welding system is extremely useful to design multimodular enzyme systems, especially to create rigid conformations that decrease the risk of intermodular interference. Further work on Jo-In will target the introduction of varying degrees of flexibility, providing the means to study this property and the way it may influence multimodular enzyme functions.

Keywords:

GH family 11 endo-1,4-β-xylanase, CBM family 2, CBM family 3, Bio Molecular Welding, spatial proximity

Abbreviations

GH – glycoside hydrolase; CBM – carbohydrate-binding module; PCW – plant cell wall; SAXS - Small angle X-ray scattering; MST - Microscale Thermophoresis; ITC - Isothermal titration calorimetry; NMR - Nuclear Magnetic Resonance; RC - regenerated cellulose; CN - cellulose nanocrystals.

Introduction

Domains constitute the key building blocks of proteins, conferring their structural integrity and/or functionalities. They can form independent structural and or functional units, but are often combined in multidomain organizations in which neighboring domains associate to define protein structures and/or functions [1]. The majority of proteins from all taxa are composed of several domains connected by linkers [2,3]. This quite complex organization is probably the source of functional diversity and also responsible for functional fine-tuning [4], including that of enzymes whose catalytic sites are often formed at the interface of several domains [5].

Plant cell wall-degrading enzymes provide excellent examples of multidomain proteins. This large group is characterized by a multitude of structures and functions, their diversity matching the complexity of plant cell wall (PCW) structures [6]. Lignified PCWs are macromolecular networks, composed of cellulose, hemicelluloses, pectins, proteins and lignins that interact and, in some cases, crosslink to form insoluble, three dimensional matrices [7]. The main enzymes involved in the breakdown of PCWs are glycoside hydrolases (GHs), a large and diverse group including cellulases, hemicellulases and pectinases. Most GHs display modular architecture, containing catalytic and non-catalytic domains [8,9]. Regarding the latter, carbohydrate binding modules (CBMs) are prominent.

When appended to a catalytic module, CBMs target specific regions in polysaccharides, consequently increasing the local concentration of catalytic domains and favoring intimate contacts between the substrate and the enzyme. In certain cases, CBMs also disrupt the surface of tightly packed polymers, such as cellulose or starch, thus facilitating enzyme action [10].

In PCW-degrading enzymes, domain organizations are numerous and quite varied. In some cases, the catalytic GH domain and the CBM are combined in a single prolonged domain, while in others the CBM is appended to the GH *via* a linker peptide of variable size (from 4 to 158 residues), composition and structure [11]. Considering the number of known GH and CBM domains and the number of possible combinations, the organizational diversity of PCW-degrading enzymes is considerable [12].

Previous studies described the creation of synthetic multimodular GH constructs [13–15] designed to investigate enzymatic activity. Often, a domain fusion strategy was adopted, using short linker sequences to associate different domains in recombinant proteins. While this strategy is frequently employed, its success hinges on expression of the fusion protein and requires the cloning and expression of each studied domain combinations. An alternative route to obtain a range of different domain combinations is to express single domains separately and then perform module linkage in a second *in vitro* step. Several strategies to achieve this have also been described [16–21]. One of the more recent additions to the protein engineer's toolbox is genetically encoded click chemistry (GECC), based on a naturally occurring phenomenon identified in bacterial pili, where certain protein subunits are linked together *via* an isopeptide bond [22]. Exploiting this for protein engineering has led to the development of SpyTag-SpyCatcher [23] and the Biomolecular Welding tool [24]. The latter

comprises two proteins, designated Jo and In (10.6 and 16.5 kDa, respectively), which spontaneously form an intramolecular isopeptide bond when mixed in solution, leading to a two-domain protein measuring 6 nm in length. When Jo and In are individually fused to other protein domains, it is possible to create domain combinations *in vitro*, with the Jo-In intramolecular complex acting as the linker. Accordingly, Jo-In were recently used to combine two different GHs, producing bifunctional enzymes [25].

In the current study, focusing on the well characterized xylanase Xyn11A from *Neocallimastix patriciarum* [26] Jo-In is used to link this GH to two different, non-cognate CBMs of bacterial origin either targeting the substrate of Xyn11A (xylan) or another PCW polymer (cellulose), the aim being to understand how the specific properties of these CBMs affect enzyme activity on simple substrates and complex PCW networks.

Materials and methods

Gene cloning

Plasmid constructs used are summarized in Supplementary Table S1. For some cloning purposes, PCR (Phusion™ High-Fidelity DNA Polymerase, ThermoFischer Scientific, Waltham, MA, USA) was used to amplify target sequences, generally introducing restriction enzyme target sequences, and to introduce PCR amplicons into linearized plasmid vectors by homologous recombination (In-Fusion® HD cloning kit, Clonetech, Mountain View, CA, USA). Alternatively, target sequences were synthesized by Genscript HK limited (Piscataway, NJ, USA) introducing appropriate restriction enzyme target sequences for subsequent plasmid construction.

Protein expression and purification

Proteins were expressed in *Escherichia coli* strain BL21 (DE3) or Tuner (DE3) harbouring the relevant plasmids and purified using standard methods described in Supplementary Table S2.

Covalent chimeric protein complexes

To prepare chimeric protein complexes, purified Jo and In fusion proteins were mixed, using a slightly lower concentration for the xylanase than for the CBMs (typically 2 µmoles of xylanase for 3 µmoles of CBM, 8.3 and 8.8 mg/ml of protein, respectively), for 1 h at 21°C and then stored overnight at 4 °C. Protein complexes were isolated from solution using a XK16 Hiload 16/600 Superdex S75 prep-grade gel filtration column (GE Healthcare Life Sciences, Chicago, IL, USA) connected to an Äkta Pure system. Elution was performed at 1 mL/min using 50 mM sodium phosphate buffer pH 7.4 supplemented with 150 mM NaCl. Subsequently, NaCl was removed by dialysis and purified chimeric complexes were judged homogenous by sodium dodecyl polyacrylamide gel electrophoresis (SDS-PAGE).

Enzymatic activity measurements

The apparent kinetic parameters K_{Mapp}, V_{max}, k_{cat}, and $k_{cat}/K_{M\ app}$ of Jo-*Np*Xyn11A were measured using the dinitrosalicylic acid (DNSA) assay as previously described [25], using various concentrations (0.3 to 30 mg/mL) of beechwood xylan (BWX, Megazyme) in activity assay buffer (50 mM sodium phosphate, 12 mM sodium citrate pH 6, supplemented with 1 mg/mL of bovine serum albumin (BSA, Merck KGaA, Darmstadt, Germany). DNSA assays were performed to determine the specific activity (SA) of xylanase derivatives (5 nM) on 0.5% (w/v) wheat arabinoxylan (WAX), 0.5% (w/v) rye arabinoxylan (RAX) or 1% (w/v) BWX respectively (all from Megazyme, Bray, Ireland) in 50 mM Tris-HCl pH 7.5, supplemented with 1 mg/mL of BSA as previously described [27]. SA of the xylanases (100

nM) was also determined using 4-nitrophenyl-β-D-xylotrioside (*p*NP-X_3, LIBIOS, France) using 5 mM of substrate in activity assay buffer as previously described [25]. SA were expressed in µmoles of product formed per min per µmole of enzyme (IU/µmole) in order to integrate the differences of mass concentration [25]. To investigate enzyme activity on complex substrates, 5 g destarched wheat bran and 10 g wheat straw (0.5 mm) (both from ARD, Pomacle, France), were each washed in 2 L of deionized water for 1 h at 4 °C and recovered by filtration (0.45 µm) before drying at 50 °C for 3 d. For enzyme assays, wheat bran or straw (2 % w/v) were incubated overnight in 1.9 mL of activity assay buffer before the addition of enzyme (final concentration 1 µM). Reactions were conducted at 37 °C under constant mixing at 1200 rpm (ThermoMixer® C, Eppendorf, Hamburg, Germany). Reaction progress was monitored by regular sampling as previously described [25]. All experiments were performed in triplicate, and the reported values are the means of three experiments ± SD. Kinetic parameters were derived from the data using the Michaelis-Menten equation embedded in SigmaPlot 11.0 (Systat Software,San Jose, CA, USA).

Isothermal titration calorimetry (ITC)

ITC measurement was carried out using a MicroCal VP-ITC titration calorimeter (Malvern Panalytical, Malvern, UK) as detailed in Supporting Information. Integrated heat effects were analyzed by non-linear regression using a single-site binding model (Microcal ORIGIN software, version 7.0, Microcal Software), yielding values for the association constant Ka (M^{-1}) and the binding enthalpy ΔH ($J.mol^{-1}$). Other thermodynamic parameters were calculated using the standard thermodynamic equation:

$-RTlnKa = \Delta G = \Delta H - T\Delta S$.

Microscale Thermophoresis (MST)

MST measurement was carried out using a Monolith NT115 (NanoTemper Technologies GmbH, München, Germany) at 25 °C, 20% LED power and 40 % MEST power as detailed in Supporting Information. Data analysis was performed with MO Affinity software 2.1 (Nanotemper). The Hill equation was chosen to determine a value for EC50 [30]. EC50 is the half-maximal effective concentration, meaning the more affinity for the substrate is, the smaller the value of the EC50 will be.

Nuclear Magnetic Resonance (NMR)

NMR experiments were performed on a Bruker Avance III HD 800 MHz spectrometer equipped with a 5 mm quadruple resonance QCI-P (H/P-C/N/D) cryogenically cooled probe head (Bruker, Billerica, MA, USA) as detailed in Supporting Information. Analysis of the data and fitting of the chemical-shift perturbation to the standard equation for a saturation isotherm was performed using SigmaPlot 11.0 (Systat Software, San Jose, CA, USA).

Small angle X-ray scattering (SAXS)

SAXS measurements were performed at Laboratoire de Génie Chimique, Toulouse, on the XEUSS 2.0 bench (Xenocs, Grenoble, France) equipped with a copper internal source (Genix3D) that produces a X-ray beam (8 keV and 30.10^6 ph.s^{-1}) providing a size resolution of approximately 500 × 500 µm. Proteins were concentrated to approximately 10 mg/mL using a centrifugal filter device (Amicon® Ultra 30 or 50K, Merck KGaA). To remove aggregates and obtain a monodisperse solution, samples (50 µL) were injected onto a size exclusion column mounted on a HPLC coupled to the SAXS. For direct analysis, sample aliquots (40 µL) were transferred from the sample holder (maintained at 18 °C using a circulating water bath) to the measurement cell placed under vacuum to limit air absorption. Data were collected on a 150 × 150 mm area DECTRIS detector (Pilatus 1M) at a sample-

detector distance of 1.216 m, thus procuring a measurement range from 0.005 to 0.5 $Å^{-1}$. Each sample dataset is an average of at least 6 measurements with a data collection time of 1,800 s. The averaged curves obtained using direct injection and SEC-HPLC were merged to obtain a composite curve devoid of an aggregation contribution at small angles and displaying low noise at high angles. Finally, to obtain the absolute scattering intensity I(q) for the solutes, the background buffer solution contribution was subtracted from the total SAXS profile. Data integration and reduction were performed using FOXTROT software. The biophysical parameters, such as gyration radius (Rg), maximal distance (Dmax) and Porod volume were calculated using PRIMUS [28] from the ATSAS suite. Low resolution shapes were calculated with DAMMIF and rigid body molecular modelling using the SAXS data was performed using CORAL.

Paraffin embedding, microtomy, on-section enzymatic digestion and double immunofluorescence labelling.

Sample preparation was performed essentially as previously described [29] with minor modifications. Briefly, wheat straw (1 cm long) and wheat bran were fixed in acetic acid/ethanol without aldehyde, infiltrated in paraplast and assembled as tissue arrays in paraplast. Tissue arrays corresponded to hundreds of wheat bran fragments and at least four wheat straw cross sections. Tissue array blocks were soaked for several weeks in acetic acid/ethanol softening solution at 4 °C [30] and 14 µm thick serial sections were displayed on silane coated slides. Individual slides were dewaxed and covered with a microincubation chamber (22×40×0.2 mm deep; (200 µL), #70324-20, Electron Microscopy Science, Hatfield, PA, USA) containing either 50 mM sodium-phosphate 12 mM citrate buffer pH 6 alone or containing enzymes (300 nM final concentration). Slides were incubated for 24 h at 37 °C in a humid atmosphere and then recombinant enzymes were digested with proteinase K (5 µg/ml

in 0.1 M Tris-HCl pH 8-50 mM EDTA pH 8) for 30 min at 37 °C. Double immunofluorescence labelling was performed as previously described [31] using xylan-specific LM11 monoclonal antibody (PlantProbes, Leeds, UK) and cellulose specific His_6-Tagged *Ct*CBM3a recombinant protein (PlantProbes, Leeds, UK) as primary probes. These were labelled with goat anti-rat IgG-Alexa Fluor 488 (ThermoFischer, Waltham, MA, USA) and His_6-Tag monoclonal antibody (4E3D10H2/E3)-Alexa Fluor 555 (ThermoFischer, Waltham, MA, USA), respectively. Slides were mounted in ProLong™ Gold Antifade mounting medium (ThermoFischer, Waltham, MA, USA) and scanned with a Nanozoomer 2.0 RS scanner (Hamamatsu photonics, Hamamatsu City, Japan) using a 40x objective and 7×1 µm Z stacks. Scans were analysed with NDP view (Hamamatsu photonics). The lignin autofluorescence observed for the A488 channel in all the cell walls from the untreated/unlabelled sections was set to a minimum threshold to observe the LM11/A488 specific labelling on the other sections. No such an autofluorescence is seen for the A555 channel. Figures were assembled using Photo-paint (Corel draw graphics suite 2018, Corel, Ottawa, Canada).

Results and Discussion

Investigating the impact of alternative multidomain arrangements on biological activity

In previous work [25] it was demonstrated how Jo and In can be used to conveniently link proteins together [24]. Therefore, Jo and In were exploited to create a series of GH-CBM chimeric proteins based on *Np*Xyn11A. The expression of His_6-tagged *Np*Xyn11A linked to either Jo or In at its *N*-terminus [27] yielded active enzymes. Data regarding In-*Np*Xyn11A is already available [27] so work was restricted to the comparison of the kinetic parameters of Jo-*Np*Xyn11A with those of wild type *Np*Xyn11A (Supplementary Table S3). Values of K_M

$_{app}$ for In-*Np*Xyn11A and Jo-*Np*Xyn11A (1.8 mg.mL^{-1} and 2.76 mg.mL^{-1}) are 2.4- and 3.7-fold higher than that of the wild type enzyme (0.75 mg.mL^{-1}), indicating that the affinity for BWX is lowered. As discussed previously [25], additions at the *N*-terminal extremity of the *Np*Xyn11A probably hinder the flexible loops that connect the β-sheets and form the catalytic pocket that accommodates glycone moieties. This is inferred by the fact that even subtle modifications in this highly conserved region lead to significant alterations in enzyme activity [32]. SAXS data (see Figure 3 below) revealed that in solution In-*Np*Xyn11A, displayed a partially unfolded conformation compared to *Np*Xyn11A. These observations can possibly be correlated with the relatively high value of the standard deviation of the kinetic parameters. Despite changes to K_{Mapp} and k_{cat}, the overall catalytic efficiency of the two chimeric enzymes and *Np*Xyn11A were similar due to compensatory effects on k_{cat} and K_{Mapp}.

To use the Jo-In system to assess rapidly the effect of covalent linkage of *Np*Xyn11A to *Ct*CBM3a and *Cf*CBM2b-1, the same strategy was used to prepare CBM chimeras, yielding the proteins Jo-CBM3a, In-CBM3a, Jo-CBM2b-1 and In-CBM2b-1. A pull down assay [33] performed using insoluble cellulose confirmed the binding ability of *Ct*CBM3a and its Jo and In derivatives (see supporting information for detailed protocol, Supplementary Figure S1). Further investigation using Isothermal titration calorimetry (ITC) and either regenerated cellulose (RC) or cellulose nanocrystals (CN) confirmed that *Ct*CBM3a showed similar K_a values in the case of both ligands (see supporting information for detailed protocol, Supplementary Figure S2). It is noteworthy that ITC data also indicate that the *Ct*CBM3a-ligand interaction is enthalpy-driven, with the entropic component being unfavorable, consistent with previous data related to CBMs binding to RC [34]. Having demonstrated that CNs constitute a suitable ligand for *Ct*CBM3a, they were used to evaluate the binding properties of Jo-CBM3a and In-CBM3a using microscale thermophoresis (MST) (see

supporting information for detailed protocol, **Table 1** and Supplementary Figure S3). Since Jo- and In-CBM3a are optimally stable in different buffers, to compare them with *Ct*CBM3a it was necessary to determine CN EC_{50} values for the latter in both buffers. Comparing Jo-CBM3a with *Ct*CBM3a revealed that the EC_{50} values were highly similar (0.21 $g.L^{-1}$ and 0.14 $g.L^{-1}$, respectively). However, the EC_{50} value characterizing the interaction of In-CBM3a with CN was 60-fold lower than that of *Ct*CBM3a (0.003 $g.L^{-1}$ and 0.18 $g.L^{-1}$, respectively), indicating a higher affinity of In-CBM3a for CN. In this respect, it is noteworthy that *Ct*CBM3a binding to CN is only moderately sensitive to buffer changes, because the difference between the two EC_{50} values was only 1.28-fold. Therefore, accounting for buffer effects, while the appendage of Jo to the *N*-terminal extremity of *Ct*CBM3a has a relatively minor impact on ligand binding, the appendage of In significantly reinforces it.

To investigate the ligand binding properties of *Cf*CBM2b-1 and its Jo and In derivatives for soluble oligosaccharides, NMR was used (see supporting information for detailed protocol). This revealed that CBM binding to X_6 significantly perturbed the chemical shift of the side chains NH^{ε} signals of two solvent exposed Trp residues (Supplementary Figure S4). Monitoring these shifts provided a K_d value for the *Cf*CBM2b-1/X_6 interaction (**Table 2**), with data being in the same order of magnitude as a previously reported value [35]. Determination of the K_d value for X_6 binding to In-CBM2b-1 gave a similar value, but in identical assay conditions no interaction (i.e. K_d > 10 mM) between Jo-CBM2b-1 and X_6 was evidenced. The reason for this difference is unknown, but clearly Jo engages in unfavorable interactions with CBM2b-1 that possibly lead to the steric hindrance of one or more of the CBM's ligand binding determinants [35].

In summary, the attachment of Jo or In to the *N*-terminus of *Np*Xyn11A yielded an active xylanase. However, attachment of these elements to the *N*-termini of *Ct*CBM3a or *Cf*CBM2b-1 yielded variable results. The attachment of In increased the binding affinity for both CBMs (significantly for CBM3a) while the attachment of Jo decreased both binding affinities (drastically for CBM2b-1). Nevertheless, despite this it was decided to proceed with the creation of Jo-In linked multimodular chimeras, because previous work has shown that the covalent association of Jo and In leads to a stable complex devoid of flexibility [24]. Similarly, it was postulated that any deleterious effects arising from the linkage of either Jo or In to a CBM might be attenuated once the Jo-In complex is formed.

Creation and biochemical characterization of multimodular chimeric enzymes

Using the different Jo and In derivatives, four multimodular chimeric xylanases were prepared and purified (**Figure 1**A-B). As shown by SDS-PAGE, the apparent molecular weight (MW) of *Np*Xyn11A-[Jo-In]-CBM3a, *Np*Xyn11A-[In-Jo]-CBM3a, *Np*Xyn11A-[Jo-In]-CBM2b-1 and *Np*Xyn11A-[In-Jo]-CBM2b-1 are consistent with predicted values, obtained by summing the MWs of the individual modules (Figure 1B, Supplementary Table S2).

Measurement of hydrolytic activity of multimodular chimeric xylanases on *p*NP-X_3, a substrate small enough to avoid major interference from the CBM, showed that all the enzymes display activities in the same order of magnitude as recombinant *Np*Xyn11A **(Table 3**). The activity of *Np*Xyn11A-[In-Jo]-CBM2b-1 was reduced by 36%, even though In-*Np*Xyn11A displayed almost the same activity as *Np*Xyn11A. Conversely, while the attachment of Jo to *Np*Xyn11A led to a 20% reduction in activity on *p*NP-X_3, adding In-CBM2b-1 restored activity to a level almost identical to that of *Np*Xyn11A. Moreover, the

316 addition of In-CBM3a was not deleterious (Table 3). These results are consistent with current
317 knowledge that the presence of CBM appendages does not enhance the activity of GHs on
318 soluble substrates such as *p*NP-glycosides or short oligosaccharides [36].
319
320 Regarding the activities of the four chimeric multimodular xylanases on soluble polymeric
321 substrates (RAX, WAX and BWX), the enzymes fall into one of two categories. When In-
322 *Np*Xyn11A is linked to either of the Jo-CBMs the activity on all three substrates is mostly
323 lower than *Np*Xyn11A, with CBM2b-1 having the most deleterious effect of up to 66% loss
324 of activity. This result could be related to the loss of binding properties of Jo-CBM2b-1
325 (Table 2) and does not follow examples in the literature suggesting that activity enhancement
326 could be expected [37]. Nevertheless, when Jo-*Np*Xyn11A is linked to either In-CBMs,
327 activity on the different substrates is mostly increased, with the exception of *Np*Xyn11A-[Jo-
328 In]-CBM2b-1 on BWX (10% activity loss) (Table 3). Remarkably, the activity of *Np*Xyn11A-
329 [Jo-In]-CBM3a on RAX was increased by 135% compared to that of *Np*Xyn11A on the same
330 substrate (2.92 ± 0.04 mM xylose equivalent and 1.25 ± 0.16 mM xylose equivalent after 15
331 min of reaction, respectively). Clearly, activity increases related to the presence of CBM2b-1
332 can be tentatively attributed to the specific ligand binding ability of the CBM. However, the
333 significant increase correlated with the presence of the cellulose-targeting CBM3a is less
334 intuitive. Nevertheless, a recent study also revealed that the appendage of a cellulose-specific
335 CBM family 1 to xylanase *Np*Xyn11C [38] increased catalytic efficiency by 21% on BWX.
336 The underlying reasons for such activity enhancements is unclear and are often treated
337 cautiously [39]. The fold and architecture of a xylanase core was proposed to explain the
338 positive effect of a CBM targeting xylan on the catalytic activity of GH family 11 towards
339 soluble xylan [37]. In the case of the present results, accounting for the relatively large MW
340 of the xylan polymers (~ 350 kDa) [27] and the shape of the chimeric enzyme (see SAXS data

below, Figure 5B), it may be postulated that non-specific interactions cannot be excluded, although with no evidence for this.

The enzymatic activity of *Np*Xyn11A derivatives was also evaluated using destarched wheat bran (DWB), which displays a high arabinoxylan:cellulose ratio [40] and wheat straw (WS), which conversely displays a low arabinoxylan:cellulose ratio [41]. After 23 h, chimeric xylanases had released ~7.5-fold more reducing sugars from DWB than from WS (**Figure 2**), consistent with the greater availability of arabinoxylan in the former and also the greater structural and chemical complexity of WS. Moreover, the presence of either CBM clearly enhanced final reducing sugar yield (by ~17% in the case of DWB), even with the presence of *Ct*CBM3a that apparently reduced the initial reaction rate (Figure 2A). The impact of the nature of the Jo-In linkage was also significant with *Np*Xyn11A-[Jo-In]-CBM2b-1 displaying a faster initial rate than *Np*Xyn11A-[In-Jo]-CBM2b-1. On WS, the presence of *Ct*CBM3a proved to be a severe handicap, because activity was ~75% lower than that of the catalytic domain alone (Figure 2B). Instead, the impact of *Ct*CBM2b-1 was imperceptible, since the activities of the *Ct*CBM2b-1 chimeras were nearly identical to that of the catalytic domain alone. However, the discriminating nature of the Jo-In linkage was again perceptible, because despite its faster initial rate, *Np*Xyn11A-[In-Jo]-CBM2b-1 generated ~15 % less reducing sugars when compared to *Np*Xyn11A-[Jo-In]-CBM2b-1. These results demonstrate the importance of substrate targeting by CBMs, especially in complex environments such as PCWs [15]. DWB provides *Cf*CBM2b-1 with an abundant source of highly accessible ligand binding sites, whereas the cellulose-specific *Ct*CBM3a probably hinders the early progression of the enzyme in this matrix. In contrast, WS provides *Ct*CBM3a with abundant crystalline cellulose. Thus, binding of *Ct*CBM3a chimeras to cellulose sequesters the enzyme and prevents it from reaching its arabinoxylan target substrate [15,42]. It is noteworthy that

366 although MST and NMR measurements revealed that In-CBM3a and Jo-CBM2b-1 display
367 impaired ligand binding (Tables 1 and 2) and experiments using purified xylan substrates
368 suggest that the activities of *Np*Xyn11A chimeras are sensitive to the exact nature of the Jo-In
369 linkage (Table 3), these factors did not appear to be major determinants of activity on
370 complex insoluble substrates.
371
372 **SAXS and NMR analysis of the multimodular xylanases**
373 As previously described [24], the anti-parallel organization of the stable complex Jo-In and
374 the possibility to link Jo or In to the *N*- and *C*-termini of proteins of interest [25] offers the
375 ability to create chimeric proteins and modulates the relative spatial orientation of linked
376 protein domains. To examine the structures of the protein chimeras created in this work,
377 SAXS data (**Figure 3**) were recorded and biophysical parameters were extracted (Figure 3C).
378 The single domain *Np*Xyn11A generated a SAXS curve typical of a globular, folded protein
379 (Figure 3A) that fits well with the theoretical curve calculated using CRYSOL and crystal
380 structure data (PDB id: 2C1F) (data not shown). However, addition of the In domain resulted
381 in a modified solution structure, with the Rg and Dmax values (46.2Å and 160Å respectively)
382 being considerably higher than those of *Np*Xyn11A (18.5Å and 60Å respectively), in
383 agreement with the increase of the MW. It appears that the In domain of In-*Np*Xyn11A is
384 present as a long unfolded tail, while the *Np*Xyn11A maintains its globular structure. SAXS
385 curves of Jo and In derivatives of *Cf*CBM2b-1 displayed the characteristics of unfolded
386 proteins with a constant decreased at medium angles (0.008 to 0.1$Å^{-1}$). The proton NMR
387 spectrum of the isolated *Cf*CBM2b-1 is characteristic of a well-folded protein domain, with
388 several methyl resonances below 0 ppm and well-defined Trp side chain signals (**Figure 4**).
389 The Jo-CBM2b-1 and In-CBM2b-1 constructs display similar resonances devoid of chemical
390 shifts or spectral broadening, indicating that the CBM domain maintains its 3D fold within

391 these constructs. Indeed, calculation of a difference spectrum (i.e. subtracting the spectrum of
392 the isolated *Cf*CBM2b-1 domain from that of the Jo/In derivatives) confirmed that the spectra
393 of the Jo/In -attached *Cf*CBM2b-1 are simple composites of the spectra of the constituent
394 proteins domains. This implies that when linked to *Cf*CBM2b-1, neither Jo nor In intrinsically
395 alter the structure of the CBM. However, the fact that Jo-CBM2b-1 binds less effectively than
396 *Cf*CBM2b-1 to X_6 (Table 2) suggests that the unstructured Jo domain obstructs access to the
397 CBM's ligand binding site. A similar conclusion possibly explains the lower activity of In-
398 *Np*Xyn11A against BWX, since the SAXS data (Figure 3) indicates that the In domain is
399 partially unstructured and might obstruct access to the catalytic site (Supplementary Table S3
400 and Table 3).
401 The second set of SAXS curves presented in Figure 3B are those of the multimodular
402 xylanases. These display a similar profile, with intensity decreasing to a plateau at small
403 angles ($q < 0.01$ Å^{-1}), corresponding to the Guinier region. At higher angles ($0.01 < q < 0.08$ Å^{-1}
404 and $0.08 < q < 0.2$ Å^{-1}) the curves decay, consistent with the power law function $I(q) = q^{-p}$, with
405 p value ≈ 2 and 4 respectively. This is characteristic of elongated proteins. For the
406 multimodular xylanases, *Np*Xyn11A-[In-Jo]-CBM2b-1 and *Np*Xyn11A-[Jo-In]-CBM2b-1,
407 the plots of P(r) *versus* r are very similar (**Figure 5**A) and reflect a multidomain, elongated,
408 global form (Figure 5B). In contrast, although the P(r) profiles of *Np*Xyn11A-[In-Jo]-CBM3a
409 and *Np*Xyn11A-[Jo-In]-CBM3a are also highly similar, they nevertheless differ from those of
410 *Np*Xyn11A-[In-Jo]-CBM2b-1 and *Np*Xyn11A-[Jo-In]-CBM2b-1, displaying more marked
411 oscillations that reflect the larger size of *Ct*CBM3a (17.1 kDa compared to 9.1 kDa for
412 CBM2b-1). Despite this difference, the curves are also indicative of elongated shapes
413 composed of distinct domains (Figure 5B). The comparison of experimental SAXS data
414 acquired for *Np*Xyn11A-[In-Jo]-CBM2b-1 and *Np*Xyn11A-[Jo-In]-CBM2b-1 with that of
415 model curves generated using crystallographic data revealed that these were highly similar,

with a goodness of fit χ^2 = 1.25 and 1.57 respectively (**Figure 6**A). For each chimera, modelling and superimposing the theoretical structure that displayed the best χ^2 value provided low-resolution hypothetical structures (Figure 6B-C). Irrespective of the Jo-In configuration, the distance between *Np*Xyn11A and *Cf*CBM2b-1 is quite similar in both models (118.0 ± 9.6Å for *Np*Xyn11A-[In-Jo]-CBM2b-1 and 120.6 ± 5.5 Å for *Np*Xyn11A-[Jo-In]-CBM2b-1). However, due to the axial asymmetry in the Jo-In complex, the torsion angle is + 66.3 ± 27.6° for *Np*Xyn11A-[In-Jo]-CBM2b-1 and -145.4 ± 21.1° for *Np*Xyn11A-[Jo-In]-CBM2b-1 (Supplemnetary Figure S6). Predictive structural modelling of *Np*Xyn11A-[In-Jo]-CBM3a and *Np*Xyn11A-[Jo-In]-CBM3a using CORAL was not possible because of significant structural variability (i.e. $\chi^2 > 2$) that prevented fitting to the molecular envelope of the SAXS data.

Differences in targeting multimodular xylanases in wheat straw

To further test the possibility of using the chimeric xylanases on raw substrate, experiments were performed *in situ* on wheat bran and wheat straw PCW sections and the accessible xylans and cellulose localization were monitored using immunological labelling. Following treatment of the wheat bran PCW sections with multimodular enzymes (*Np*Xyn11A-[Jo-In]-CBM3a was omitted from this study), LM11/A488-specific xylan labelling between the pericarp and the nucellar epidermis (**Figure 7** C1-F1) and intense continuous CBM3a/A555-specific labelling of the nucellar epidermis (Figure 7 C2-F2) were observed. This contrasts with the untreated sections that displayed no LM11/A488 labelling and only faint CBM3a/A555 labelling (Figure 7B). Although increased labelling after enzymatic treatment appears counter intuitive, it is almost certainly a consequence of PCW complexity. The action of the chimeric xylanases leads to the removal of xylan and concomitant exposure of hitherto masked PCW components, such as cellulose and xylan, which constitute new ligands for antibody or CBM binding. However, experiments performed on DWB failed to reveal any

major changes to labelling. Therefore, subsequent work focused on WS (**Figure 8**, Supplementary Figures S7 and S8). The use of either probe on untreated sections produced homogenous labelling of both PCW components (Figure 8B). However, after treatment with *Np*Xyn11A (Figure 8C) and *Np*Xyn-[Jo-In]-CBM2b-1 (Figure 8D), LM11/A488 labelling was repeatedly found to be diminished when observing different vascular bundles (Supplementary Figure S7). This suggests that the presence of CBM2b-1 did not enhance the activity of *Np*Xyn11A on WS. Additionally, compared to *Np*Xyn11A, *Np*Xyn-[Jo-In]-CBM2b-1 was apparently less active on intervascular fibres. Finally, diminution of the CBM3a/A555 labelling (cellulose-specific probe) was correlated with xylan hydrolysis. Conversely, treatment with *Np*Xyn11A-[In-Jo]-CBM2b-1 or *Np*Xyn11A-[In-Jo]-CBM3a generally did not affect LM11/A488 labelling intensity (Figure 8E-F; Supplementary Figure S7), although this was strongly enhanced in patches around the phloem, the protoxylem and in vascular bundle cell corners. In distal zones, intense patches of LM11/A488 labelling were also observed in sclerenchyma cell corners and around the pith parenchyma intercellular spaces (Supplementary Figure S8). For PCW sections treated with *Np*Xyn11A-[In-Jo]-CBM2b-1, additional patches of LM11/A488 labelling were also observed in the intervascular fibres, but this was not the case when *Np*Xyn11A-[In-Jo]-CBM3a was used (Figure 8E-F; Supplementary Figure S7). The impact on cellulose labelling was also more evident for *Np*Xyn11A-[In-Jo]-CBM2b-1 than for *Np*Xyn11A-[In-Jo]-CBM3a (Figure 8E-F; Supplementary Figure S7).

Previously, both *Ct*CBM3a and *Cf*CBM2b-1 were shown to potentiate the activity of a cognate xylanase on tobacco PCWs, presumably by improving its substrate targeting capability [15]. However, the present results do not confirm this and may signify limited usefulness for the Jo-In system when studying enzyme activity on complex matrices, even

466 though the structural environment of xylan and xylan-cellulose interactions are different in
467 tobacco PCW [43]. It can be postulated that Jo-In introduces a high degree of rigidity
468 compared to natural linkers found in PCW-degrading enzymes. While rigidity might be
469 undesirable in certain circumstances, it can be useful in others. Specifically, greater protein
470 rigidity will be useful in investigating different spatial organizations in multidomain proteins,
471 locking chimeric protein isoforms in different domain configurations.
472
473 **Conclusions**
474 A previous study on *Ct*CBM3a linked to endoglucanase CelA of *Clostridium*
475 *thermocellum* revealed that the CBM must be correctly oriented to potentiate enzymatic
476 activity, especially on insoluble substrates [44]. In this regard, the nature of the linker is
477 certainly important because its structure will strongly contribute to the spatial orientations of
478 linked protein domains. Here, the Jo-In complex has been used to link protein domains, the
479 resultant linker complexes being stable, rather rigid protein structures. The first implication of
480 this rigidity is the likelihood that there will be no physical interference between the attached
481 protein domains. In the case of *Np*Xyn11A linked to CBMs, this is certainly the case because
482 the solution structures are elongated and characterized by well separated GH and CBM
483 domains. The second implication is that the spatial orientation (torsion angle) of the two
484 linked proteins domains is locked. If this is optimal then synergy should be possible and
485 enhancement of the activity of the GH domain will be a likely outcome. Conversely, if this is
486 suboptimal, the chimera will be definitively impaired, lacking sufficient linker flexibility to
487 allow alternative solution conformers. Accordingly, it is proposed that data related to the
488 hydrolysis of insoluble substrates described herein reflects this fact, revealing that
489 *Np*Xyn11A-[Jo-In]-CBM2b-1 has a more optimal configuration for hydrolysis than
490 *Np*Xyn11A-[In-Jo]-CBM2b-1. The third implication of linker rigidity is that protein chimeras

are likely to encounter difficulty in penetrating structurally complex three-dimensional matrices. In this work, the fact that the addition of CBMs to *Np*Xyn11A failed to potentiate the hydrolysis of wheat straw possibly supports this hypothesis.

In summary, this work confirms the usefulness of the Jo-In system in creating multidomain GHs. However, one caveat is the intrinsic rigidity of Jo-In. When designing chimeric proteins, this property must be considered with respect to the intended purpose.

Acknowledgements

We thank Pr. Harry Gilbert (ICMB, Newcastle University) for providing access and expertise in ITC experiments. We also thank Dr. Jean Jacques Bono and Virginie Gasciolli (LIPM, Toulouse) for providing access and expertise in MST experiments. The imaging using Nanozoomer RS was performed at the FR-AIB imaging platform of TRI-genotoul facility (Toulouse). We thank Dr. Gianluca Cioci for technical assistance with FPLC provided by the ICEO facility dedicated to enzyme screening and discovery, part of the Integrated Screening Platform of Toulouse (PICT, IBiSA).

Author contributions

LB, VB, CYM conceived and designed the experiments. LB, PR, TE, GL, IV and CYM performed the experiments. LB, VB, PR, GL, MJO and CYM analyzed the data. LB, MJO and CYM wrote the paper.

References

[1] Wang Y, Zhang H, Zhong H, Xue Z. Protein domain identification methods and online resources. Comput Struct Biotechnol J 2021;19:1145–53. https://doi.org/10.1016/j.csbj.2021.01.041.

[2] Apic G, Gough J, Teichmann SA. Domain combinations in archaeal, eubacterial and eukaryotic proteomes. J Mol Biol 2001;310:311–25. https://doi.org/10.1006/jmbi.2001.4776.

[3] Apic G, Huber W, Teichmann SA. Multi-domain protein families and domain pairs: comparison with known structures and a random model of domain recombination. J Struct Funct Genomics 2003;4:67–78. https://doi.org/10.1023/A:1026113408773.

[4] Altschuh D, Tessier DC, Vernet T. Modulation of the enzymatic activity of papain by interdomain residues remote from the active site. Protein Eng Des Sel 1994;7:769–76. https://doi.org/10.1093/protein/7.6.769.

[5] Valentini G, Chiarelli L, Fortin R, Speranza ML, Galizzi A, Mattevi A. The Allosteric Regulation of Pyruvate Kinase. J Biol Chem 2000;275:18145–52. https://doi.org/10.1074/jbc.M001870200.

[6] Lombard V, Golaconda Ramulu H, Drula E, Coutinho PM, Henrissat B. The carbohydrate-active enzymes database (CAZy) in 2013. Nucleic Acids Res 2014;42:D490–5. https://doi.org/10.1093/nar/gkt1178.

[7] Amos RA, Mohnen D. Critical review of plant cell wall matrix polysaccharide glycosyltransferase activities verified by heterologous protein expression. Front Plant Sci 2019;10. https://doi.org/10.3389/fpls.2019.00915.

[8] Wu H, Ioannou E, Henrissat B, Montanier CY, Bozonnet S, O'Donohue MJ, et al. Multimodularity of a GH10 Xylanase Found in the Termite Gut Metagenome. Appl Environ Microbiol 2021;87. https://doi.org/10.1128/AEM.01714-20.

[9] Henrissat B, Davies GJ. Glycoside Hydrolases and Glycosyltransferases. Families, Modules, and Implications for Genomics. Plant Physiol 2000;124:1515–9. https://doi.org/10.1104/pp.124.4.1515.

[10] Shoseyov O, Shani Z, Levy I. Carbohydrate binding modules: biochemical properties

and novel applications. Microbiol Mol Biol Rev 2006;70:283–95. https://doi.org/10.1128/MMBR.00028-05.

[11] Sammond DW, Payne CM, Brunecky R, Himmel ME, Crowley MF, Beckham GT. Cellulase linkers are optimizedbBased on domain type and function: insights from sequence analysis, biophysical measurements, and molecular simulation. PLoS One 2012;7:e48615. https://doi.org/10.1371/journal.pone.0048615.

[12] Sidar A, Albuquerque ED, Voshol GP, Ram AFJ, Vijgenboom E, Punt PJ. Carbohydrate binding modules: diversity of domain architecture in amylases and cellulases from filamentous microorganisms. Front Bioeng Biotechnol 2020;8. https://doi.org/10.3389/fbioe.2020.00871.

[13] Pasari N, Adlakha N, Gupta M, Bashir Z, Rajacharya GH, Verma G, et al. Impact of Module-X2 and Carbohydrate Binding Module-3 on the catalytic activity of associated glycoside hydrolases towards plant biomass. Sci Rep 2017;7:3700. https://doi.org/10.1038/s41598-017-03927-y.

[14] Cuskin F, Flint JE, Gloster TM, Morland C, Basle A, Henrissat B, et al. How nature can exploit nonspecific catalytic and carbohydrate binding modules to create enzymatic specificity. Proc Natl Acad Sci 2012;109:20889–94. https://doi.org/10.1073/pnas.1212034109.

[15] Herve C, Rogowski A, Blake AW, Marcus SE, Gilbert HJ, Knox JP. Carbohydrate-binding modules promote the enzymatic deconstruction of intact plant cell walls by targeting and proximity effects. Proc Natl Acad Sci 2010;107:15293–8. https://doi.org/10.1073/pnas.1005732107.

[16] Shah NH, Muir TW. Inteins: nature's gift to protein chemists. Chem Sci 2014;5:446–61. https://doi.org/10.1039/C3SC52951G.

[17] Pinto F, Thornton EL, Wang B. An expanded library of orthogonal split inteins enables

modular multi-peptide assemblies. Nat Commun 2020;11:1529. https://doi.org/10.1038/s41467-020-15272-2.

[18] Zhao X, Scheffner M, Marx A. Assembly of branched ubiquitin oligomers by click chemistry. Chem Commun 2019;55:13093–5. https://doi.org/10.1039/C9CC07303E.

[19] You C, Piehler J. Multivalent chelators for spatially and temporally controlled protein functionalization. Anal Bioanal Chem 2014;406:3345–57. https://doi.org/10.1007/s00216-014-7803-y.

[20] Singh S, Kluger R. Self-Assembly of a Functional Triple Protein: Hemoglobin-Avidin-Hemoglobin via Biotin–Avidin Interactions. Biochemistry 2016;55:2875–82. https://doi.org/10.1021/acs.biochem.6b00215.

[21] Fierobe H-P, Mechaly A, Tardif C, Belaich A, Lamed R, Shoham Y, et al. Design and Production of Active Cellulosome Chimeras. J Biol Chem 2001;276:21257–61. https://doi.org/10.1074/jbc.M102082200.

[22] Sun F, Zhang W-B. Unleashing chemical power from protein sequence space toward genetically encoded “click” chemistry. Chinese Chem Lett 2017;28:2078–84. https://doi.org/10.1016/j.cclet.2017.08.052.

[23] Zakeri B, Fierer JO, Celik E, Chittock EC, Schwarz-Linek U, Moy VT, et al. Peptide tag forming a rapid covalent bond to a protein, through engineering a bacterial adhesin. Proc Natl Acad Sci 2012;109:E690–7. https://doi.org/10.1073/pnas.1115485109.

[24] Bonnet J, Cartannaz J, Tourcier G, Contreras-Martel C, Kleman JP, Morlot C, et al. Autocatalytic association of proteins by covalent bond formation: a Bio Molecular Welding toolbox derived from a bacterial adhesin. Sci Rep 2017;7:43564. https://doi.org/10.1038/srep43564.

[25] Enjalbert T, De La Mare M, Roblin P, Badruna L, Vernet T, Dumon C, et al. Characterisation of the effect of the spatial organisation of hemicellulases on the

hydrolysis of plant biomass polymer. Int J Mol Sci 2020;21:4360. https://doi.org/10.3390/ijms21124360.

[26] Vardakou M, Dumon C, Murray JW, Christakopoulos P, Weiner DP, Juge N, et al. Understanding the structural basis for substrate and inhibitor recognition in eukaryotic GH11 xylanases. J Mol Biol 2008;375:1293–305. https://doi.org/10.1016/j.jmb.2007.11.007.

[27] Montanier CY, Fanuel M, Rogniaux H, Ropartz D, Di Guilmi A-M, Bouchoux A. Changing surface grafting density has an effect on the activity of immobilized xylanase towards natural polysaccharides. Sci Rep 2019;9:5763. https://doi.org/10.1038/s41598-019-42206-w.

[28] Konarev P V., Volkov V V., Sokolova A V., Koch MHJ, Svergun DI. PRIMUS : a Windows PC-based system for small-angle scattering data analysis. J Appl Crystallogr 2003;36:1277–82. https://doi.org/10.1107/S0021889803012779.

[29] Badruna L, Burlat V, Montanier CY. CBMs as probes to explore plant cell wall heterogeneity using immunocytochemistry, 2017, p. 181–97. https://doi.org/10.1007/978-1-4939-6899-2_14.

[30] Brandizzi F. Plant microtechnique and microscopy. vol. 86. 2000. https://doi.org/10.1006/anbo.2000.1231.

[31] Francoz E, Ranocha P, Le Ru A, Martinez Y, Fourquaux I, Jauneau A, et al. Pectin demethylesterification generates platforms that anchor peroxidases to remodel plant cell wall domains. Dev Cell 2019;48:261-276.e8. https://doi.org/10.1016/j.devcel.2018.11.016.

[32] Song L, Siguier B, Dumon C, Bozonnet S, O'Donohue MJ. Engineering better biomass-degrading ability into a GH11 xylanase using a directed evolution strategy. Biotechnol Biofuels 2012;5:3. https://doi.org/10.1186/1754-6834-5-3.

[33] Crouch LI, Labourel A, Walton PH, Davies GJ, Gilbert HJ. The Contribution of non-catalytic carbohydrate binding modules to the activity of lytic polysaccharide monooxygenases. J Biol Chem 2016;291:7439–49. https://doi.org/10.1074/jbc.M115.702365.

[34] Boraston AB. The interaction of carbohydrate-binding modules with insoluble non-crystalline cellulose is enthalpically driven. Biochem J 2005;385:479–84. https://doi.org/10.1042/BJ20041473.

[35] Simpson PJ, Bolam DN, Cooper A, Ciruela A, Hazlewood GP, Gilbert HJ, et al. A family IIb xylan-binding domain has a similar secondary structure to a homologous family IIa cellulose-binding domain but different ligand specificity. Structure 1999;7:853–64. https://doi.org/10.1016/S0969-2126(99)80108-7.

[36] Tomme P, Tilbeurgh H, Pettersson G, Damme J, Vandekerckhove J, Knowles J, et al. Studies of the cellulolytic system of Trichoderma reesei QM 9414. Analysis of domain function in two cellobiohydrolases by limited proteolysis. Eur J Biochem 1988;170:575–81. https://doi.org/10.1111/j.1432-1033.1988.tb13736.x.

[37] Kittur FS, Mangala SL, Rus'd AA, Kitaoka M, Tsujibo H, Hayashi K. Fusion of family 2b carbohydrate-binding module increases the catalytic activity of a xylanase from Thermotoga maritima to soluble xylan. FEBS Lett 2003;549:147–51. https://doi.org/10.1016/S0014-5793(03)00803-2.

[38] Zhang Y, Yang H, Yu X, Kong H, Chen J, Luo H, et al. Synergistic effect of acetyl xylan esterase from Talaromyces leycettanus JCM12802 and xylanase from Neocallimastix patriciarum achieved by introducing carbohydrate-binding module-1. AMB Express 2019;9:13. https://doi.org/10.1186/s13568-019-0740-6.

[39] Hoffmam ZB, Zanphorlin LM, Cota J, Diogo JA, Almeida GB, Damásio ARL, et al. Xylan-specific carbohydrate-binding module belonging to family 6 enhances the

641 catalytic performance of a GH11 endo-xylanase. N Biotechnol 2016;33:467–72.
642 https://doi.org/10.1016/j.nbt.2016.02.006.
643 [40] Bouraoui H, Desrousseaux M-L, Ioannou E, Alvira P, Manaï M, Rémond C, et al. The
644 GH51 α-l-arabinofuranosidase from Paenibacillus sp. THS1 is multifunctional,
645 hydrolyzing main-chain and side-chain glycosidic bonds in heteroxylans. Biotechnol
646 Biofuels 2016;9:140. https://doi.org/10.1186/s13068-016-0550-x.
647 [41] Motte J-C, Escudié R, Beaufils N, Steyer J-P, Bernet N, Delgenès J-P, et al.
648 Morphological structures of wheat straw strongly impacts its anaerobic digestion. Ind
649 Crops Prod 2014;52:695–701. https://doi.org/10.1016/j.indcrop.2013.11.038.
650 [42] Gao D, Chundawat SPS, Sethi A, Balan V, Gnanakaran S, Dale BE. Increased enzyme
651 binding to substrate is not necessary for more efficient cellulose hydrolysis. Proc Natl
652 Acad Sci 2013;110:10922–7. https://doi.org/10.1073/pnas.1213426110.
653 [43] Busse-Wicher M, Gomes TCF, Tryfona T, Nikolovski N, Stott K, Grantham NJ, et al.
654 The pattern of xylan acetylation suggests xylan may interact with cellulose microfibrils
655 as a twofold helical screw in the secondary plant cell wall of Arabidopsis thaliana.
656 Plant J 2014;79:492–506. https://doi.org/10.1111/tpj.12575.
657 [44] Sajjad M, Khan MIM, Zafar R, Ahmad S, Niazi UHK, Akhtar MW. Influence of
658 positioning of carbohydrate binding module on the activity of endoglucanase CelA of
659 Clostridium thermocellum. J Biotechnol 2012;161:206–12.
660 https://doi.org/10.1016/j.jbiotec.2012.05.023.
661 [45] Wilkins MR, Gasteiger E, Bairoch A, Sanchez J-C, Williams KL, Appel RD, et al.
662 Protein identification and analysis tools in the ExPASy Server. 2-D Proteome Anal.
663 Protoc., New Jersey: Humana Press; n.d., p. 531–52. https://doi.org/10.1385/1-59259-
664 584-7:531.
665 [46] Fumagalli M, Ouhab D, Boisseau SM, Heux L. Versatile gas-phase reactions for

surface to bulk esterification of cellulose microfibrils aerogels. Biomacromolecules 2013;14:3246–55. https://doi.org/10.1021/bm400864z.

[47] Wu H, Montanier CY, Dumon C. Quantifying CBM carbohydrate interactions using microscale thermophoresis, 2017, p. 129–41. https://doi.org/10.1007/978-1-4939-6899-2_10.

[48] Kaufmann M, Klinger C, editors. Functional Genomics. vol. 815. New York, NY: Springer New York; 2012. https://doi.org/10.1007/978-1-61779-424-7.

[49] Millard P, Lippens G. Interact: Automated analysis of protein-ligand interactions by 1D and 2D NMR. BioRxiv 2018:215194. https://doi.org/10.1101/215194.

Legends to Figures and Tables

Figure 1: (A) Representation of the proteins studied in this work. The multimodular enzymes are linked *via* an isopeptide bond between the Lys191 of Jo and the Asp695 of In (double fine black line). Although Jo and In are fused at the *N*-termini of *Np*Xyn11A and the CBMs respectively, the covalent Jo-In or In-Jo association between the GH and the CBM is shown in square brackets for simplicity. (B) SDS-PAGE of the protein used in this study. Lanes: M, molecular markers; 1, *Np*Xyn11A; 2, Jo-*Np*Xyn11A; 3, *Ct*CBM3a; 4, Jo-CBM3a; 5, *Np*Xyn11A-[In-Jo]-CBM3a; 6, *Cf*CBM2b-1; 7, Jo-CBM2b-1; 8, In-CBM2b-1; 9, *Np*Xyn11A-[In-Jo]-CBM2b-1; 10, *Np*Xyn11A-[Jo-In]-CBM2b-1. For illustration 11, *Np*Xyn11A-[Jo-In]-CBM3a; 12, In-CBM3a. Original gels are provided in Supplementary Information (Figure S5).

Figure 2. Degradation of complex substrates by *Np*Xyn11A and derivatives thereof. (A) Wheat bran. (B) Wheat straw. Enzyme reactions were conducted in 50 mM sodium phosphate, 12 mM sodium citrate pH6, supplemented with 1 mg/ml BSA, at 37°C. Enzyme loading was at 1 µM. Substrate concentration was at 2% w/v.

Figure 3: (A) SAXS data recorded for *Np*Xyn11A, In-*Np*Xyn11A, In-CBM2b-1 and Jo-CBM2b-1. (B) SAXS data recorded for *Np*Xyn11A-[In-Jo]-CBM2b-1, *Np*Xyn11A-[Jo-In]-CBM2b-1, *Np*Xyn11A-[In-Jo]-CBM3a and *Np*Xyn11A-[Jo-In]-CBM3a. (C) Table summarizing all parameters extracted from the Guinier plot and pair-atom distribution function P(r) such as gyration radius Rg and maximum internal distance Dmax. The folding state deduced from the parameters and the shape of the curves are also mentioned in the table for each fragment.

Figure 4: 1D proton spectrum of (A) isolated *Cf*CBM2b-1 (bottom, black), of In-CBMb2-1 (middle, red) and the difference spectrum (*Cf*CBM2b-1 – In-CBMb2-1) (top, green). (B) Isolated *Cf*CBM2b-1 (bottom, black), of Jo-CBMb2-1 (middle, red) and the difference spectrum (*Cf*CBM2b-1 – Jo-CBMb2-1) (top, orange).

Figure 5: (A) Pair distribution function calculated from SAXS data of *Np*Xyn11A-[In-Jo]-CBM2b-1 and *Np*Xyn11A-[Jo-In]-CBM2b-1 (blue and red curves respectively) and from SAXS data of *Np*Xyn11A-[In-Jo]-CBM3a and *Np*Xyn11A-[Jo-In]-CBM3a (green and yellow curves respectively). The P(r) function is plotted as P(r)/Pmax(r) *vs* distance r in order to compare the different curves by normalizing with Pmax(r). (B) Low resolution shape calculated with the DAMMIF program from ATSAS suite for the four constructs. The shapes are built with Pymol in mesh representation and filled with transparent spheres.

715

716 **Figure 6**: (A) Comparison of experimental curves generated using *Np*Xyn11A-[In-Jo]-
717 CBM2b-1 and *Np*Xyn11A-[Jo-In]-InCBM2b-1 and the theoretical curves (dotted black line)
718 calculated using CRYSOL and crystallographic data. (B) Models of *Np*Xyn11A-[In-Jo]-
719 CBM2b-1 and (C) *Np*Xyn11A-[Jo-In]-InCBM2b-1 were calculated using the CORAL
720 program. In both models, Jo-In are coloured red and green respectively. *Np*Xyn11A is in cyan
721 and *Ct*CBM2b-1in yellow. Catalytic residues of *Np*Xyn11A and residues involved in ligand
722 binding recognition of *Ct*CBM2b-1 are represented by red lines. The domains and the linker
723 are modelled with Pymol using cartoon and grey sphere representations respectively.

724

725 **Figure 7**: Double immunofluorescence of paraffin-embedded wheat bran serial sections
726 showing the impact of enzymatic on-section treatment on accessible xylan and cellulose
727 immunolabelling. Serial sections of wheat bran were incubated for 24 h using the xylanase
728 derivatives as labelled on the images and further used for double indirect immunofluorescence
729 using LM11 (xylan specific antibody) and His_6-CBM3a (cellulose specific CBM) as primary
730 probes and anti-rat IgG-Alexa 488 and anti-His_6-Alexa 555, respectively. The individual
731 fluorescence channels are shown in the two first rows as labelled, and the merge of both
732 fluorescence channels with the bright field channel is shown is the third row. Arrowheads:
733 pericarp/nucellar epidermis interface; Bars: 300 µm.

734

735 **Figure 8**: Double immunofluorescence of paraffin-embedded wheat straw serial sections
736 showing the impact of enzymatic on-section treatment on xylan and cellulose
737 immunolabelling. Serial sections of wheat straw were incubated for 24 h using the
738 recombinant xylanase derivatives as labelled on the images and further used for double
739 indirect immunofluorescence using LM11 (xylan specific antibody) and His_6-CBM3a

740 (cellulose specific CBM) as primary probes and anti-rat IgG-Alexa 488 and anti-His_6-Alexa
741 555, respectively. The individual fluorescence channels are shown as labelled for a wide field
742 view (two left rows) and for a vascular bundle magnified view (two right rows). Note, that to
743 enable fair comparison between the treatment/controls, the same zones on the different serial
744 sections are displayed. Note also that an intermediate magnification is shown for this vascular
745 bundle in the ROI of Supplementary Figure S7, as well as two additional ROIs. bsf, bundle
746 sheath fibres; cp, cortical parenchyma zones; ep, epidermis; if, intervascular fibres; mx,
747 metaxylem; p, pith; ph, phloem; pp, pith parenchyma; px, protoxylem; s, sclerenchyma; vb,
748 vascular bundle. Bars: 250 µm (two left rows); 25 µm (two right rows).
749
750
751
752 **Table 1**: Binding affinity of *Ct*CBM3a and derivates against cellulose nanocrystals. Buffer 1:
753 50 mM Tris HCl pH 7.4, 150 mM NaCl, 10 mM $MgCl_2$, 0.05 % Tween 20. Buffer 2: 50 mM
754 sodium phosphate buffer, pH 7 and 0.05 % pluronic acid. See Supplementary Figure S3 for
755 chart. EC_{50} is the half-maximal effective concentration, i.e. the higher the affinity for the
756 substrate, the smaller the value of the EC_{50} .
757
758 **Table 2**: Ligand affinities of *Cf*CBM2b-1, In-CBM2b-1 and Jo-CBM2b-1 for xylohexaose as
759 measured by 1D NMR by titrating the resonances of the NHε of Trp 259 and Trp 291.
760 Experiments were conducted in 50 mM sodium phosphate pH 7 at 298 °K.
761
762 **Table 3**: Specific activity of *Np*Xyn11A and derivatives, as single enzymes or in complex.
763 Reactions were performed in 50 mM sodium phosphate, 12 mM sodium citrate pH 6,
764 supplemented with 1mg/mL BSA, at 37°C. Substrate concentrations were 5 mM 4-

765 nitrophenyl-β-D-xylotrioside (*p*NP-X_3), 0.5% w/v wheat arabinoxylan (WAX), 0.5% w/v rye
766 arabinoxylan (RAX) and 1% w/v beechwood xylan (BWX). The values are shown as means ±
767 standard deviation of replicate n = 3.
768

A

	Protein name	Protein scheme	Position in Fig.2B
Single proteins	*Np*Xyn11A	N *Np*Xyn11A C	1
	*Ct*CBM3a	N CBM3a C	3
	*Cf*CBM2b-1	N CBM2b-1 C	6
Jo/In fusion proteins	In-*Np*Xyn11A	N In *Np*Xyn11A C	-
	Jo-*Np*Xyn11A	N Jo *Np*Xyn11A C	2
	In-CBM3a	N In CBM3a C	12
	Jo-CBM3a	N Jo CBM3a C	4
	In-CBM2b-1	N In CBM2b-1 C	8
	Jo-CBM2b-1	N Jo CBM2b-1 C	7
	His-Tag	Linker	
Multi-modular enzymes	*Np*Xyn11A-[In-Jo]-*CBM3a*	C CBM3a Jo N; N In *Np*Xyn11A C	5
	*Np*Xyn11A-[Jo-In]-CBM3a	C CBM3a In N; N Jo *Np*Xyn11A C	11
	*Np*Xyn11A-[In-Jo]-CBM2b-1	C CBM2b-1 Jo N; N In *Np*Xyn11A C	9
	*Np*Xyn11A-[Jo-In]-CBM2b-1	C CBM2b-1 In N; N Jo *Np*Xyn11A C	10

B

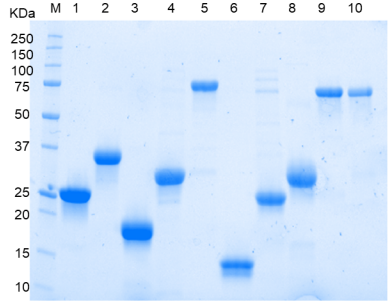

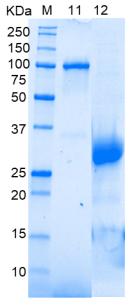

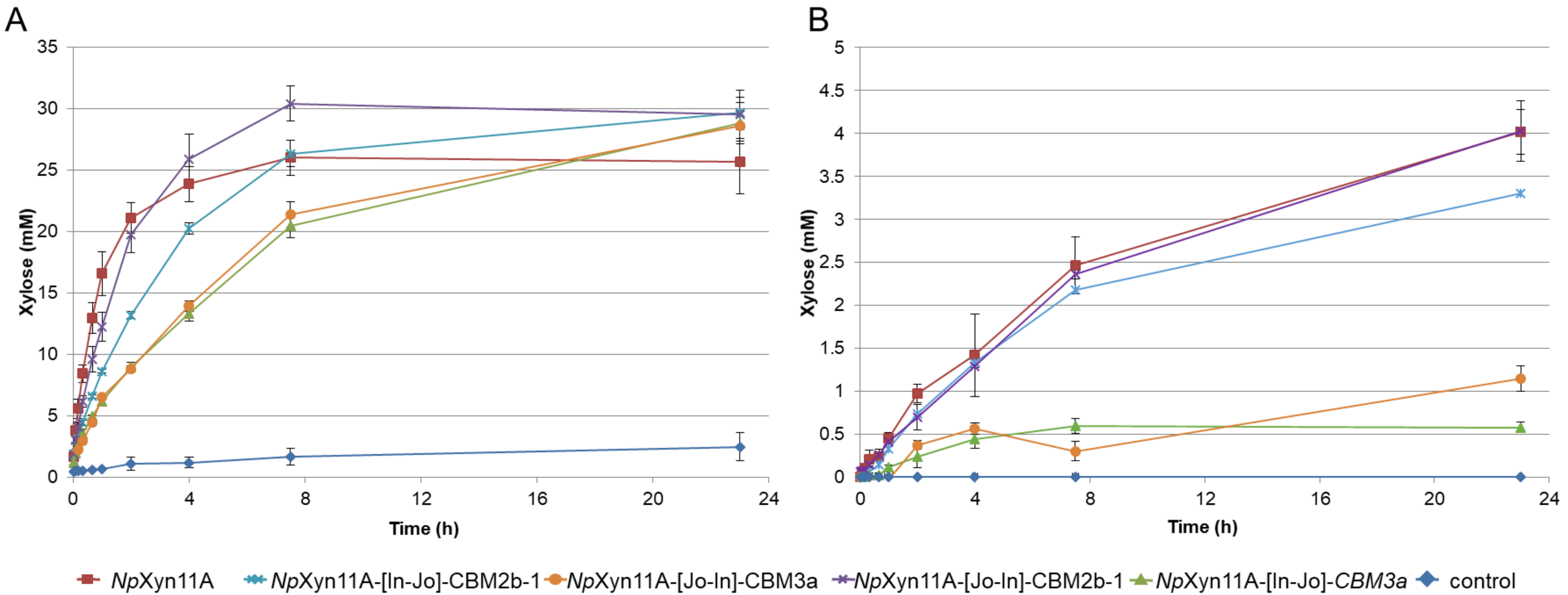
A
B
Xylose (mM)
Time (h)
0
4
8
12
16
20
24
5
10
15
20
25
30
35
0.5
1
1.5
2
2.5
3
3.5
4
4.5
NpXyn11A
NpXyn11A-[In-Jo]-CBM2b-1
NpXyn11A-[Jo-In]-CBM3a
NpXyn11A-[Jo-In]-CBM2b-1
NpXyn11A-[In-Jo]-CBM3a
control

A

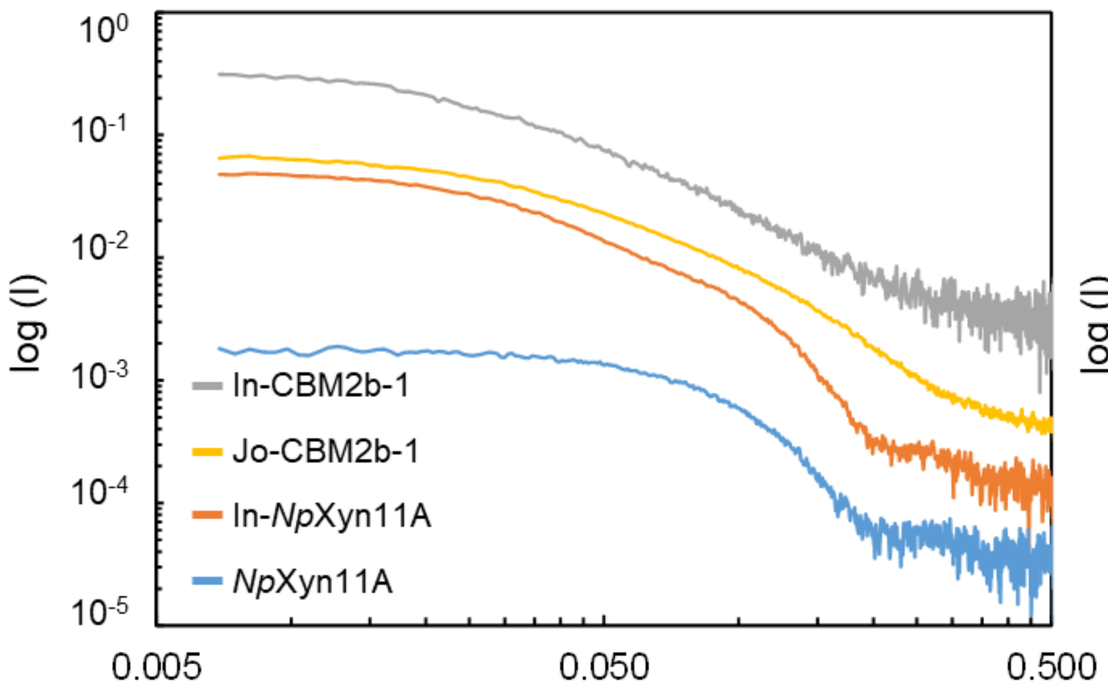

B

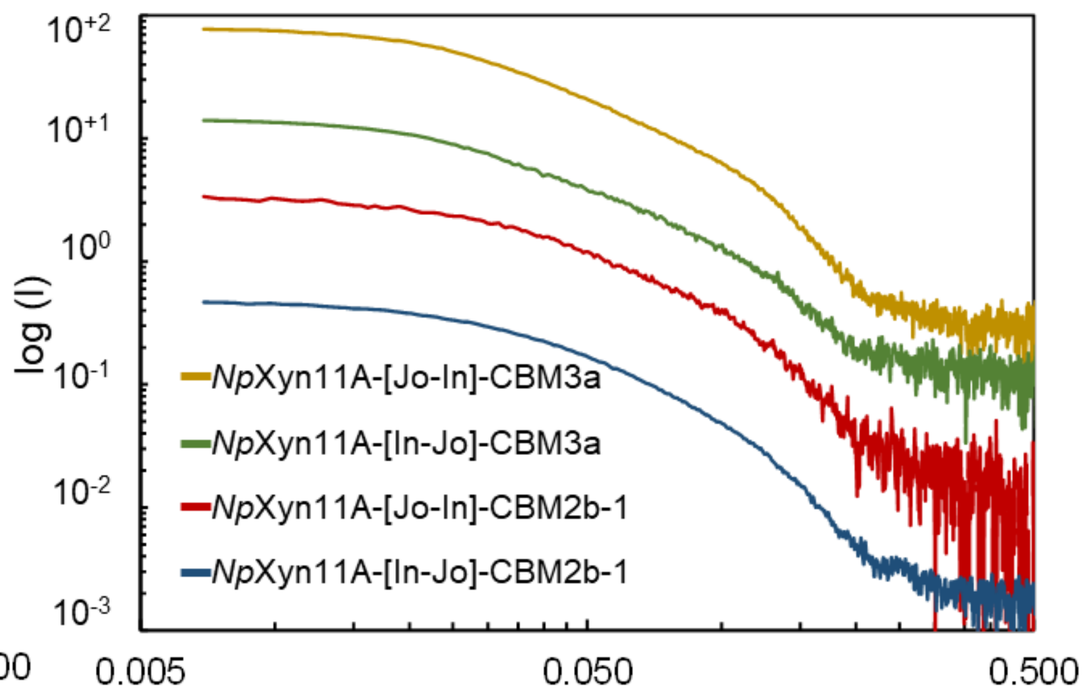

C

Sample	Molecular Mass (Kda)	Gyration radius Rg (Å)	Maximal distance D (Å)	Folding
*Np*Xyn11A-[Jo-In]-CBM3a	71.7	47.8	185	Folded
*Np*Xyn11A-[In-Jo]-CBM3a	71.0	46.5	180	Folded
*Np*Xyn11A-[Jo-In]-CBM2b-1	63.4	42.1	160	Folded
*Np*Xyn11A-[In-Jo]-CBM2b-1	62.7	41.8	150	Folded
Jo-CBM2b-1	21.1	46.1	190	Unfolded
In-CBM2b-1	27.0	58.0	210	Unfolded
In-*Np*Xyn11A	41.5	46.2	160	Partially Folded
*Np*Xyn11A	25.9	18.5	60	Folded

A

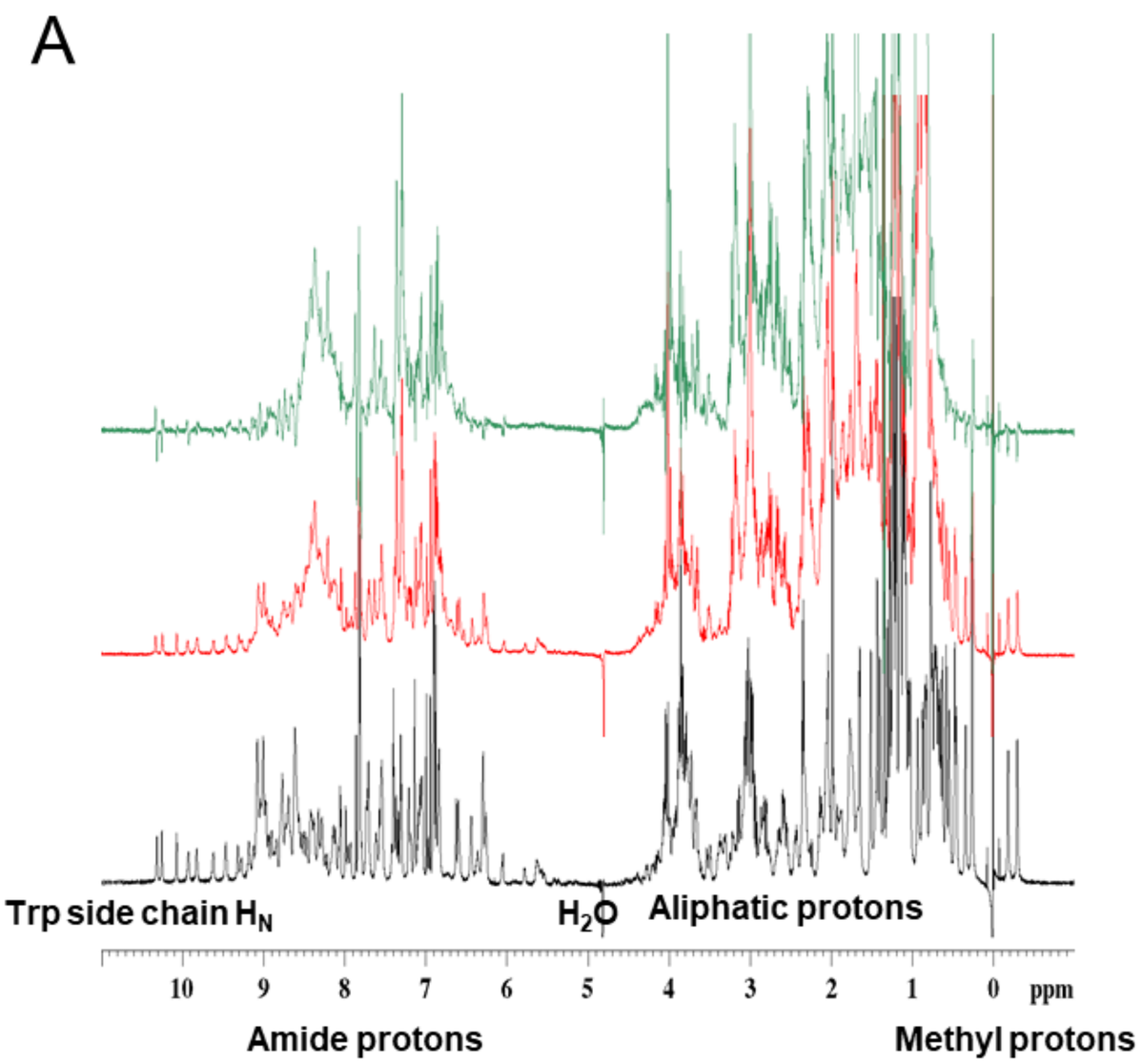
Trp side chain H_N
H_2O
Aliphatic protons
10 9 8 7 6 5 4 3 2 1 0 ppm
Amide protons
Methyl protons

B

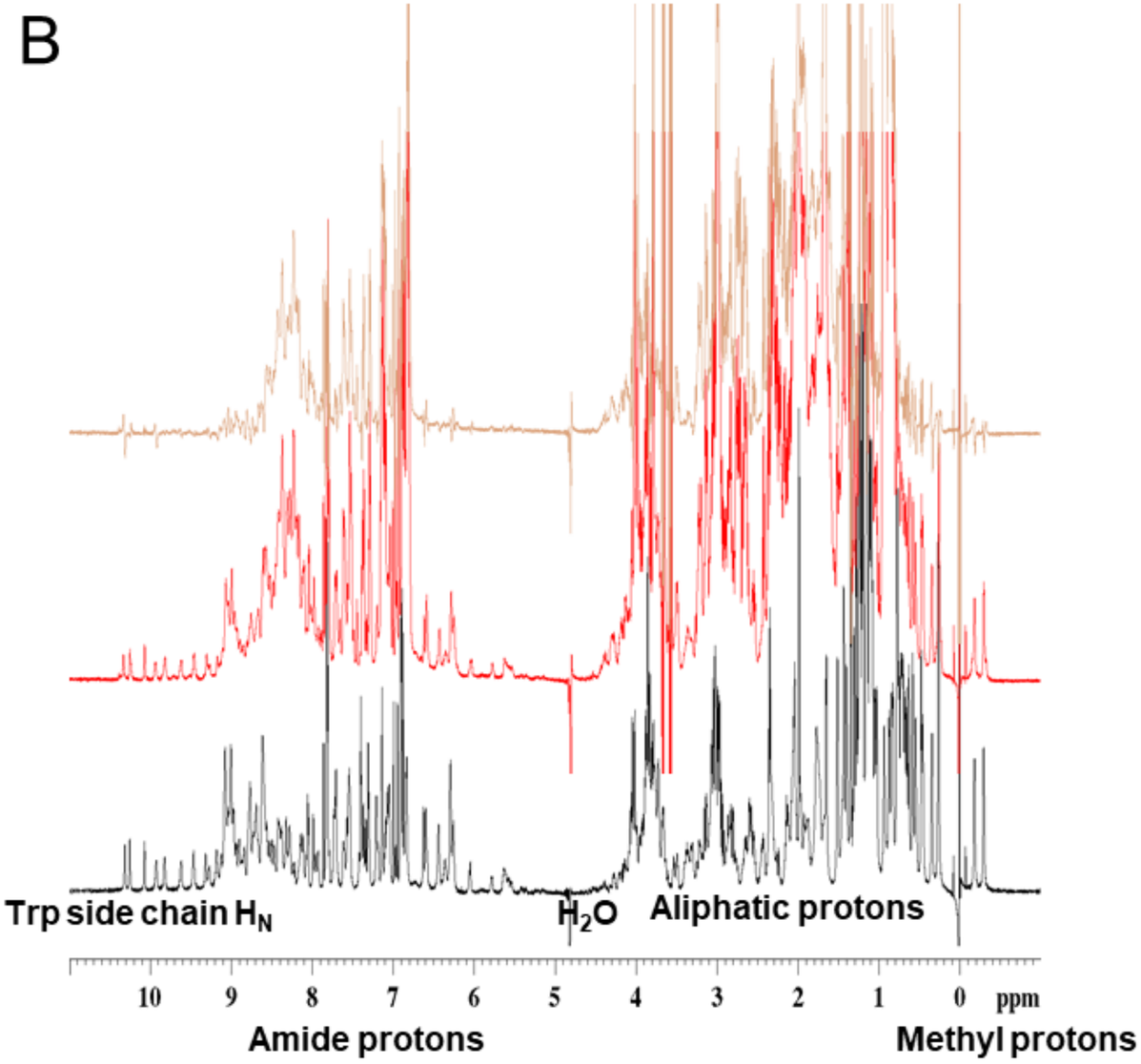
Trp side chain H_N
H_2O
Aliphatic protons
10 9 8 7 6 5 4 3 2 1 0 ppm
Amide protons
Methyl protons

A

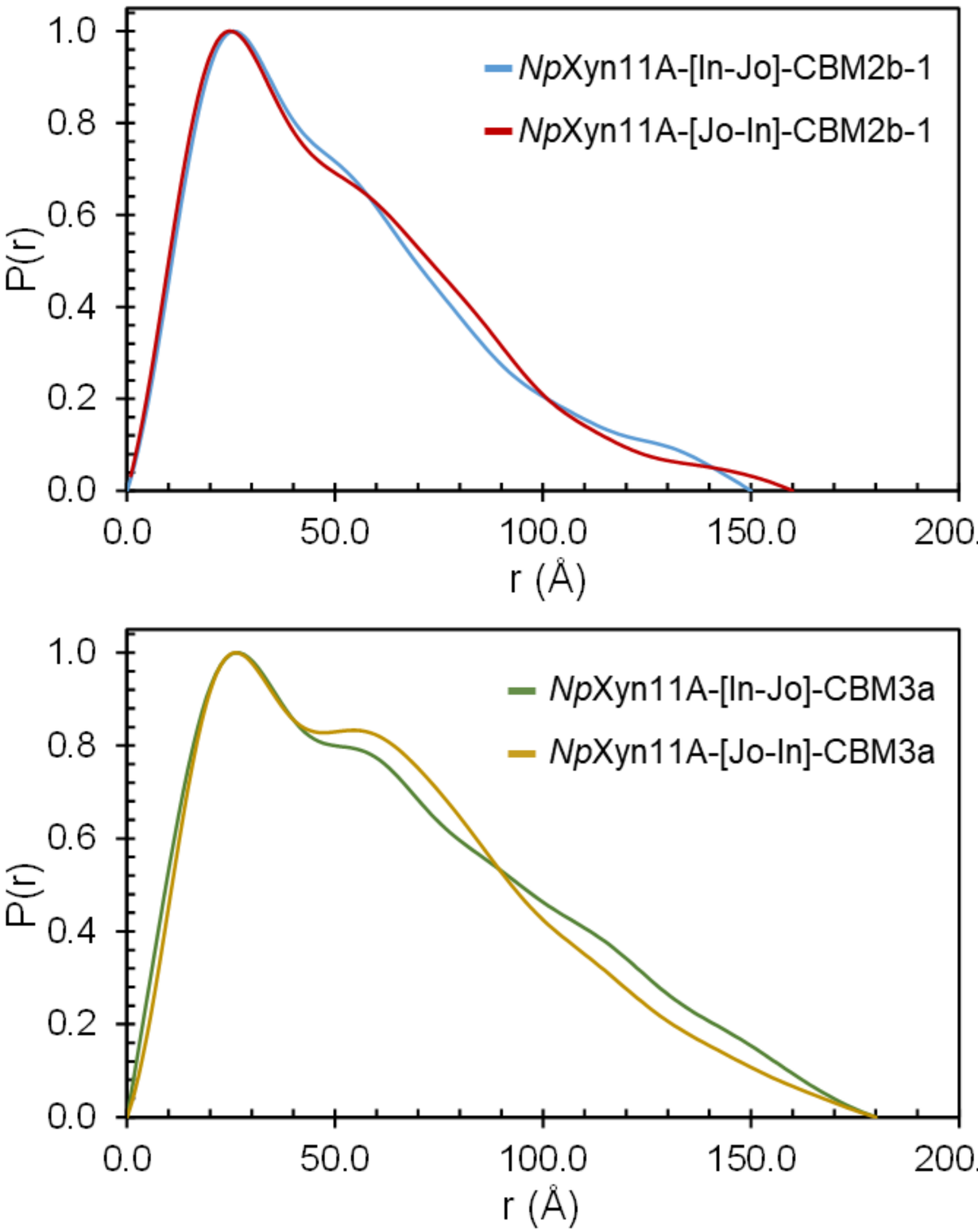
1.0
0.8
0.6
0.4
0.2
0.0
P(r)
0.0
50.0
100.0
150.0
200.0
r (Å)
NpXyn11A-[In-Jo]-CBM2b-1
NpXyn11A-[Jo-In]-CBM2b-1
NpXyn11A-[In-Jo]-CBM3a
NpXyn11A-[Jo-In]-CBM3a

B

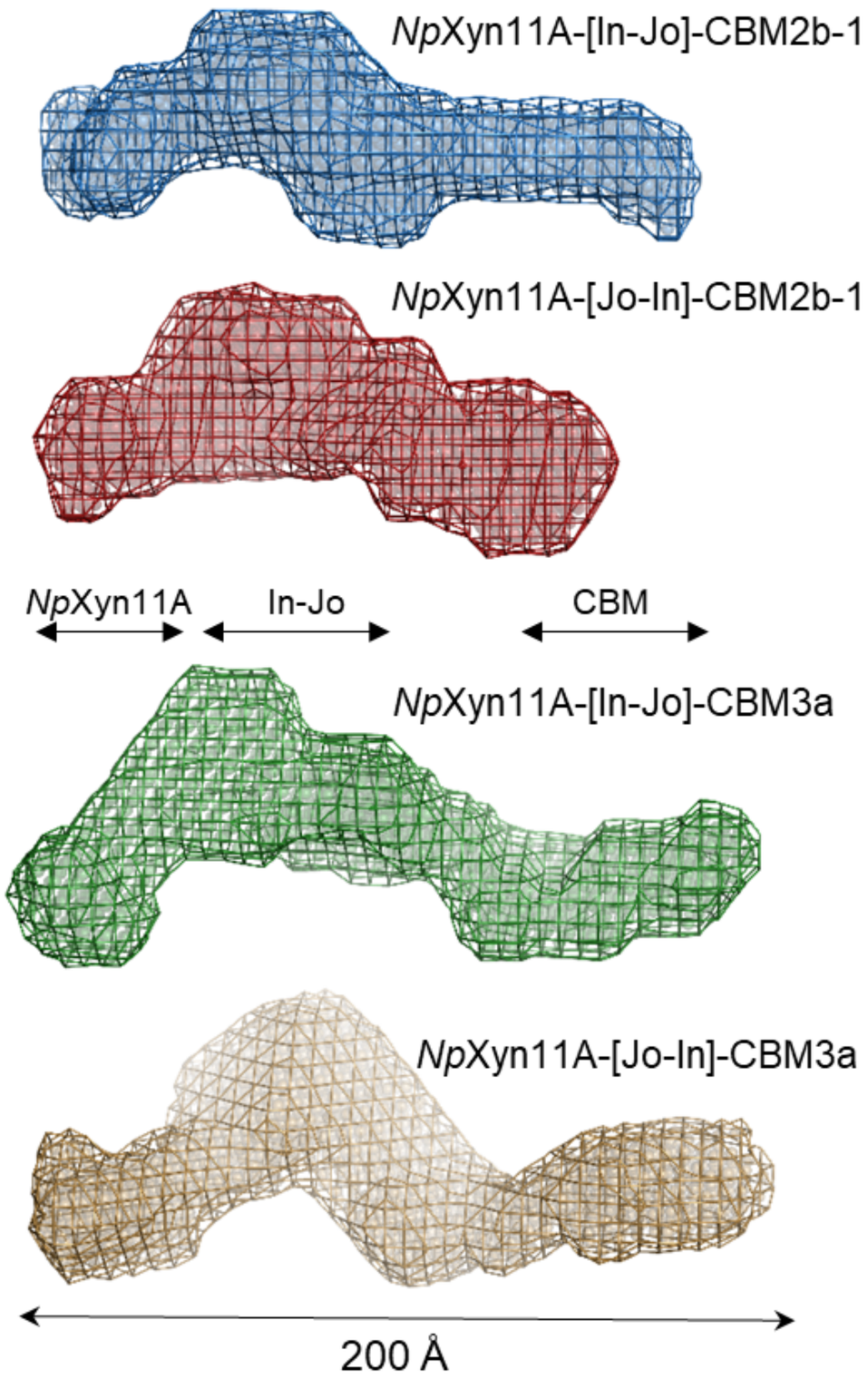
NpXyn11A-[In-Jo]-CBM2b-1
NpXyn11A-[Jo-In]-CBM2b-1
NpXyn11A
In-Jo
CBM
NpXyn11A-[In-Jo]-CBM3a
NpXyn11A-[Jo-In]-CBM3a
200 Å

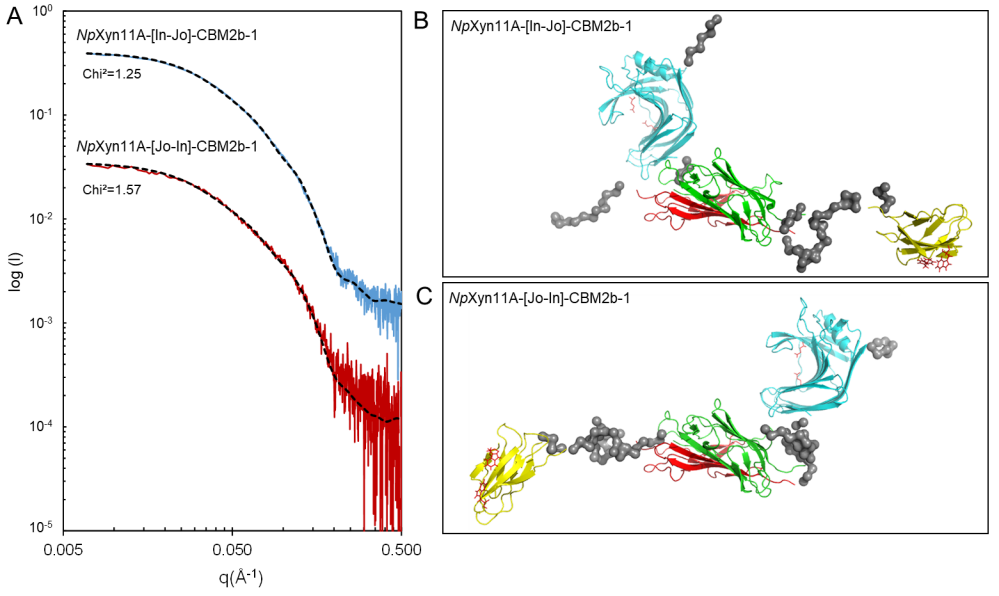
A
B
C
NpXyn11A-[In-Jo]-CBM2b-1
Chi²=1.25
NpXyn11A-[Jo-In]-CBM2b-1
Chi²=1.57
log (I)
q(Å-1)
0.005
0.050
0.500
NpXyn11A-[In-Jo]-CBM2b-1
NpXyn11A-[Jo-In]-CBM2b-1

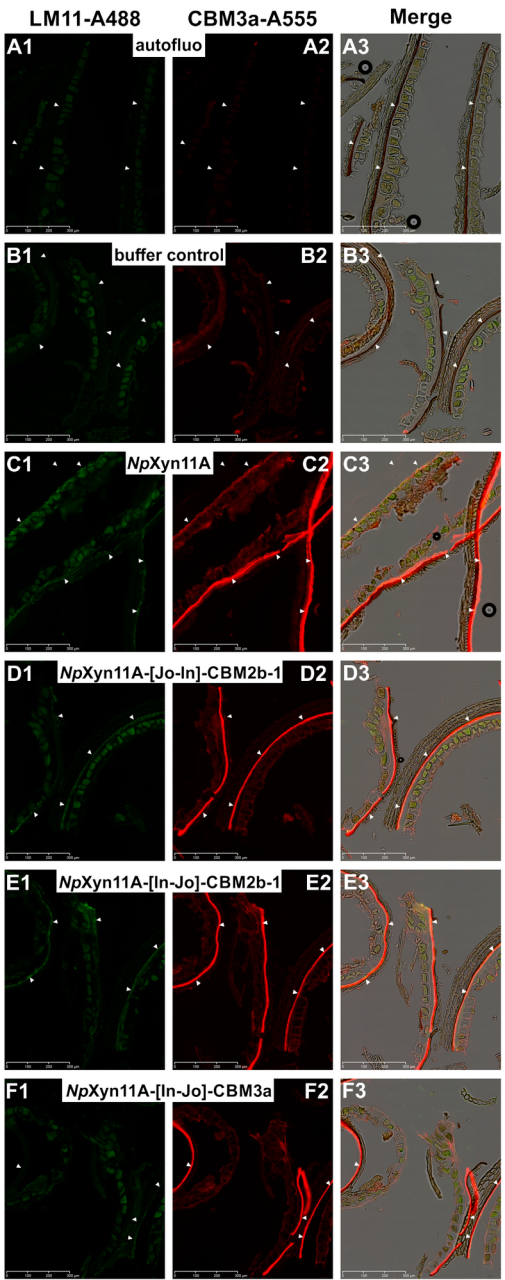
LM11-A488
CBM3a-A555
Merge
A1
autofluo
A2
A3
B1
buffer control
B2
B3
C1
NpXyn11A
C2
C3
D1
NpXyn11A-[Jo-In]-CBM2b-1
D2
D3
E1
NpXyn11A-[In-Jo]-CBM2b-1
E2
E3
F1
NpXyn11A-[In-Jo]-CBM3a
F2
F3

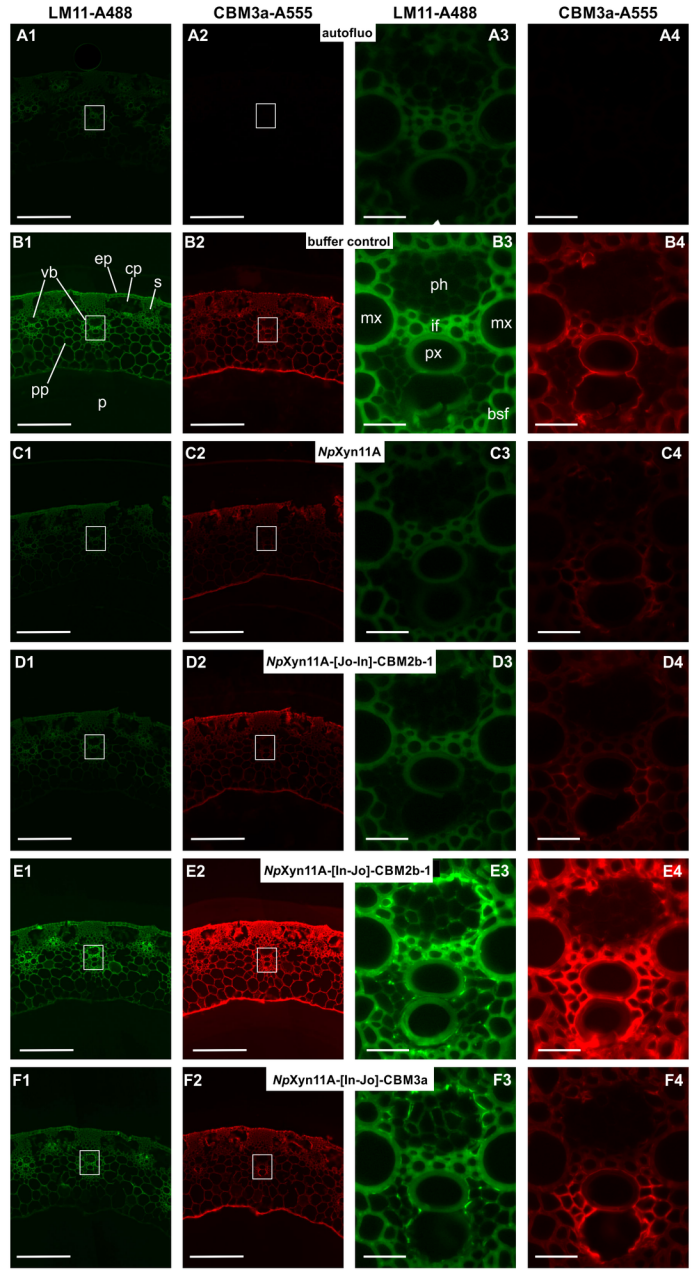
LM11-A488
CBM3a-A555
LM11-A488
CBM3a-A555
A1
A2
autofluo
A3
A4
B1
B2
buffer control
B3
B4
vb
ep
cp
s
pp
p
ph
mx
if
mx
px
bsf
C1
C2
NpXyn11A
C3
C4
D1
D2
NpXyn11A-[Jo-In]-CBM2b-1
D3
D4
E1
E2
NpXyn11A-[In-Jo]-CBM2b-1
E3
E4
F1
F2
NpXyn11A-[In-Jo]-CBM3a
F3
F4

Table 1:

Protein	EC_{50} ($g.L^{-1}$)	
	Buffer 1	*Buffer 2*
In-CBM3a	-	0.003 ± 0.0001
*Ct*CBM3a	0.14 ± 0.01	0.18 ± 0.04
Jo-CBM3a	0.21 ± 0.12	-

Table 2:

Protein	K_d (mM)		
	This work (Trp 259)	This work (Trp 291)	[35]
*Cf*CBM2b-1	0.84	1.02	0.29
In-CBM2b-1	0.22	0.52	-
Jo-CBM2b-1	> 10	> 10	-

Table 3:

Single enzymes	Specific Activity			
	***p*NP-X$_3$** (IU/µmole)	**WAX** 10^3 (IU/µmole)	**RAX** 10^3 (IU/µmole)	**BWX** 10^3 (IU/µmole)
*Np*Xyn11A	155.78 ± 4.07	114.59 ± 2.67	83.44 ± 8.21	65.03 ± 2.19
In-*Np*Xyn11A	153.17 ± 1.68	-	-	-
Jo-*Np*Xyn11A	124.63 ± 3.64	-	-	-
*Np*Xyn11A-[In-Jo]-CBM3a	148.83 ± 14.19	87.29 ± 6.32	81.58 ± 3.03	53.30 ± 0.70
*Np*Xyn11A-[Jo-In]-CBM3a	115.88 ± 25.78	160.72 ± 6.34	196.17 ± 0.60	93.40 ± 1.34
*Np*Xyn11A-[In-Jo]-CBM2b-1	98.87 ± 4.01	62.81 ± 8.28	28.57 ± 3.03	39.50 ± 0.61
*Np*Xyn11A-[Jo-In]-CBM2b-1	153.01 ± 5.30	126.91 ± 9.05	93.86 ± 9.59	58.30 ± 2.29

① Jo-In welding system = chimeric multi-modular enzyme

② Spatial orientation relatively locked

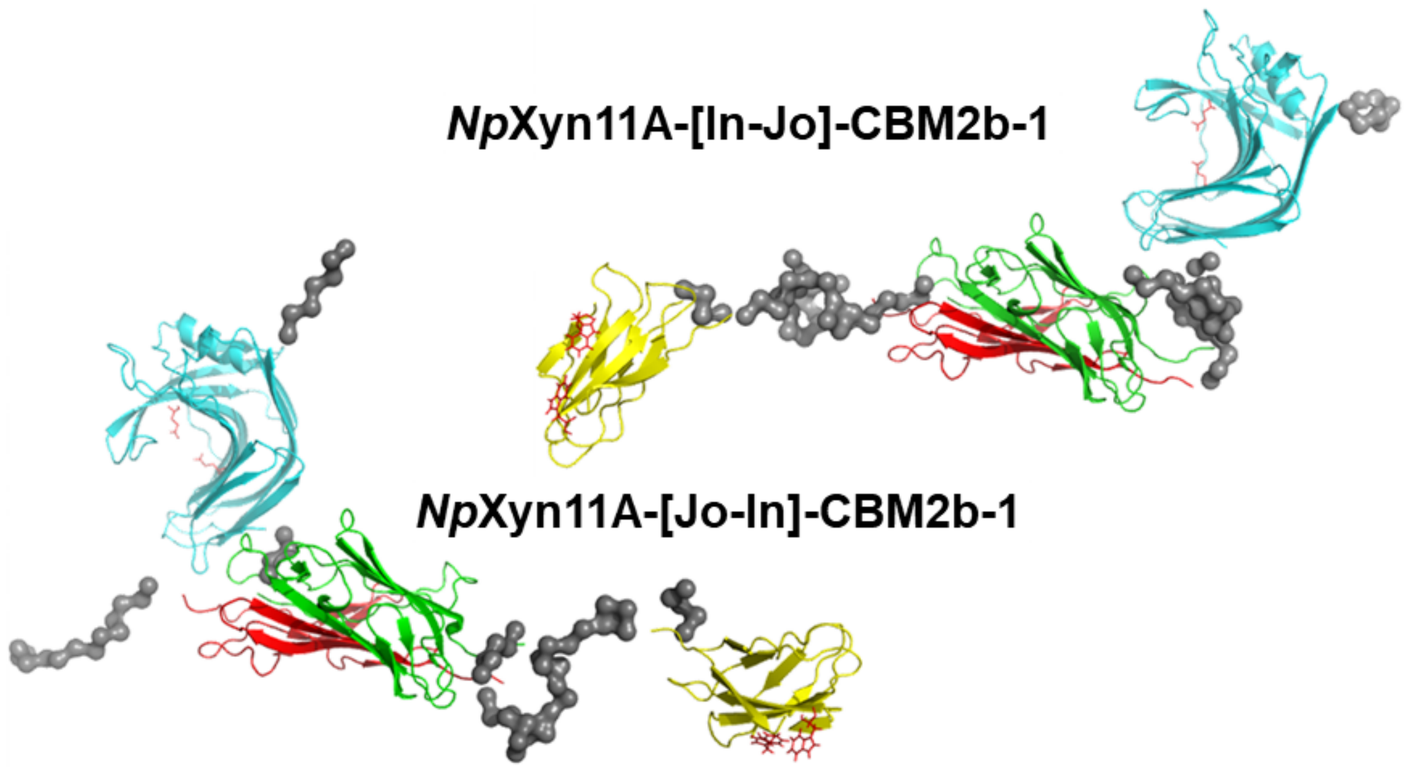

③ Optimal configuration in plant cell wall degradation